JOURNAL OF GUIDANCE, CONTROL, AND DYNAMICS
Vol. 20, No. 1, January–February 1997

Entry Guidance and Trajectory Control for Reusable Launch Vehicle

Ping Lu*
Iowa State University, Ames, Iowa 50011-3231

An entry guidance concept, similar to that of the Space Shuttle, is considered for the reusable launch vehicle (RLV). But the reference trajectory defined by drag profile is parameterized and optimized as piecewise linear functions of the energy. Analytical expressions for accurate downrange distance prediction and a performance index, the accumulated heat load, are obtained. A regularization technique is employed to achieve desired properties of the optimal drag profile. These results enable fast design of constrained optimal trajectories for both off-line studies and possible onboard application. A nonlinear control law is derived for trajectory tracking, which guarantees globally asymptotically stable tracking of the reference drag profile. Numerical results for a conceptual RLV are provided to demonstrate the optimal design of drag profiles and the performance of the trajectory control law under a variety of off-nominal conditions and navigation errors in altitude rate.

I. Introduction

AN important focus of the current effort in developing a next-generation launch system is on the reusable launch vehicle (RLV) concept (e.g., the X-33 program and also Ref. 1 and the references therein). The introduction of a reusable, single-stage launch vehicle could greatly reduce the launch costs. This paper studies an entry guidance scheme for such a vehicle.

The entry guidance problem is concerned with providing steering commands to control the entry trajectory from the atmospheric penetration to a target point where the vehicle has sufficient energy for approach and landing. The Shuttle entry guidance is highly successful for the Shuttle operations.[2,3] The Shuttle guidance concept is to design a reference drag acceleration profile as a piecewise analytical function of Earth-relative velocity (and the last segment is a function of the energy). The downrange distance can then be analytically predicted, and the reference drag profile is adjusted as necessary for updated ranging along the trajectory. A linear, time-varying, feedback control law is used to track the reference drag profile. More recently, a trajectory optimization approach is investigated in Ref. 4. In Ref. 5, Ronneke and Markl propose to schedule the drag profile as functions of the energy for the entire trajectory for more accurate range prediction, and the reference profile is then parameterized by cubic splines and determined by numerical optimization. For trajectory control, they employ a linear feedback control law whose gains are scheduled with respect to the energy. A nonlinear control law based on the feedback linearization method is compared with the Shuttle trajectory control law in Ref. 6.

Given the success of the Shuttle entry guidance scheme, it would appear most logical that the entry guidance for the RLV would adopt a similar concept, maintaining all of the strengths of the Shuttle guidance. At the same time, incorporation of the results of recent research and the increased capabilities of avionics into the RLV guidance scheme may well further improve the performance, provide greater flexibility, and increase the control capability to accommodate contingencies and larger operating domain.

We also propose to design the reference drag profile as a function of the energy, specifically, a piecewise-linear, continuous function of the energy. This seemingly trivial difference, however, brings a remarkable advantage to the design of an optimal reference profile: not only the analytical range prediction is preserved, but the performance index, the accumulated heat load, can also be evaluated analytically. This is very attractive for onboard determination of the optimal reference drag profile because no numerical integrations are involved. The essential aspects of the approach are described in Sec. II, and a regularization technique is used in Sec. III to achieve desired smooth property of the reference drag profiles. In Sec. IV, examples of the optimal drag profiles subject to some typical entry constraints for an RLV are presented. Then a nonlinear feedback trajectory control law based on a predictive control method is derived in Sec. V. Globally asymptotically stable tracking of the reference profile is established, and some potential advantages of the control law in implementation are discussed. Section VI contains simulation results on the tracking performance of the control law under a variety of off-nominal conditions and navigation errors in altitude rate. Section VII concludes the work.

II. Determination of Optimal Drag Acceleration Profiles

We begin with the standard point-mass dimensionless equations of motion in the vertical plane for the RLV over a spherical, nonrotating Earth:

$$\dot{r} = V \sin\gamma \tag{1}$$

$$\dot{V} = -D - (\sin\gamma / r^2) \tag{2}$$

$$\dot{\gamma} = [V^2 - (1/r)](\cos\gamma / Vr) + (D/V)u \tag{3}$$

where r is the radial distance from the center of the Earth to the RLV, normalized by the radius of the Earth $R_0 = 6{,}378{,}000$ m. The Earth-relative velocity V is normalized by $\sqrt{(g_0 R_0)}$, where $g_0 = 9.81$ m/s^2. The flight-path angle is γ, and the dimensionless drag acceleration $D(g)$. The differentiation is with respect to a dimensionless time $\tau = t/\sqrt{(R_0/g_0)}$. The control u is defined to be

$$u = (C_L/C_D)\cos\sigma \tag{4}$$

where C_L and C_D are the aerodynamic lift and drag coefficients, respectively, and σ is the bank angle.

To design the reference drag acceleration profile for a given downrange distance from the entry to the landing site, Ref. 5 proposes to parameterize the drag profile by cubic spline functions of the negative specific energy

$$e = (1/r) - (V^2/2) \tag{5}$$

Hereafter, e is referred to as the energy throughout. One major advantage of using e to schedule D rests on the fact that $\cos\gamma \approx 1$ is a much better approximation than $\sin\gamma \approx 0$ for moderate values of $|\gamma|$ (for instance, when $\gamma = 6$ deg, $\sin\gamma = 0.1045$, whereas $\cos\gamma = 0.9945$). As a result, the range prediction based on the drag

---

Received July 31, 1995; revision received Sept. 19, 1996; accepted for publication Sept. 21, 1996. Copyright © 1996 by the American Institute of Aeronautics and Astronautics, Inc. All rights reserved.

*Associate Professor, Department of Aerospace Engineering and Engineering Mechanics. Associate Fellow AIAA.

profile is more accurate as compared to the prediction based on the drag profile scheduled with velocity. This is because the downrange distance s, normalized by R_0, satisfies the equation

$$\dot{s} = V\cos\gamma \tag{6}$$

Since by its definition $\dot{e} = DV$, it follows that $\mathrm{d}s/\mathrm{d}e = \cos\gamma/D$, and for $\cos\gamma \approx 1$,

$$s \approx \int_{e_0}^{e_f} \frac{1}{D(e)}\,\mathrm{d}e \tag{7}$$

gives a very accurate range approximation.

We choose to represent the reference drag acceleration profile by continuous, piecewise-linear functions of e. Divide the interval $[e_0, e_f]$ into $n-1$ subintervals by the points $\{e_1, e_2, \ldots, e_n\}$ with $e_1 = e_0$ and $e_n = e_f$. In each interval $[e_i, e_{i+1}]$, $i = 1, \ldots, n-1$, let

$$D(e) = a_i(e - e_i) + b_i \tag{8}$$

where

$$a_i = \frac{D_{i+1} - D_i}{e_{i+1} - e_i}, \qquad b_i = D_i \tag{9}$$

The values of D_i, $i = 1, \ldots, n$, are to be determined. With the parametrization (8), the range can be integrated analytically from Eq. (7) to have

$$s = \sum_{i=1}^{n-1} \Delta s_i \tag{10}$$

with

$$\Delta s_i = \begin{cases} (1/a_i)\ln(D_{i+1}/D_i), & a_i \neq 0 \\ (1/D_i)(e_{i+1} - e_i), & a_i = 0 \end{cases} \tag{11}$$

The nodal values D_i are then selected to satisfy the specified range requirement by Eq. (10) and minimize a performance index, which is proportional to the accumulated heat load

$$J_0 = \int_{\tau_0}^{\tau_f} \sqrt{\rho}V^3\,\mathrm{d}\tau \tag{12}$$

where ρ is the atmospheric density. By $\mathrm{d}\tau = \mathrm{d}e/DV$ and $D = 0.5\,R_0 S C_D \rho V^2/m$ (S = reference area and m = mass of the RLV), the performance index J_0 is then proportional to

$$J^* = \int_{e_0}^{e_f} \frac{V}{\sqrt{D(e)}}\,\mathrm{d}e \approx \sqrt{2}\int_{e_0}^{e_f} \sqrt{\frac{1/\bar{r} - e}{D(e)}}\,\mathrm{d}e \tag{13}$$

where, with r approximated by an average value $\bar{r}$, the relationship $V \approx \sqrt{[2(1/\bar{r} - e)]}$ has been used. Also, a constant C_D is assumed in arriving at Eq. (13). This is accurate for most part of the entry trajectory because the angle of attack is usually held at constant from the beginning of the entry flight to a point where $e \approx 0.85$ (as is the case for the Shuttle). Toward the end of the trajectory when the angle of attack is scheduled to vary for handover to terminal area guidance, Eq. (13) is only approximately proportional to Eq. (12).

Again using the piecewise-linear parametrization (8), letting $\bar{r} = 1$ for simplicity, and defining $d_i = D_i - a_i e_i$, we have the analytical expression for J^*

$$J^* = \sqrt{2}\sum_{i=1}^{n-1}\int_{e_i}^{e_{i+1}} \sqrt{\frac{1-e}{a_i e + d_i}}\,\mathrm{d}e = \sqrt{2}\sum_{i=1}^{n-1}\Delta J_i \tag{14}$$

where

$$\Delta J_i = \begin{cases} (1/a_i)\left[\sqrt{D_{i+1}(1-e_{i+1})} - \sqrt{D_i(1-e_i)}\right] \\ \quad -\left[(a_i + d_i)\big/\sqrt{a_i^3}\right] \\ \quad \times\left[\tan^{-1}\sqrt{a_i(1-e_{i+1})/D_{i+1}}\right. \\ \quad \left. -\tan^{-1}\sqrt{a_i(1-e_i)/D_i}\right], & a_i > 0 \\ (2/3\sqrt{D_i})\left[\sqrt{(1-e_i)^3} - \sqrt{(1-e_{i+1})^3}\right], \\ & a_i = 0 \\ (1/a_i)\left[\sqrt{D_{i+1}(1-e_{i+1})} - \sqrt{D_i(1-e_i)}\right] \\ \quad +\left[(a_i + d_i)\big/\sqrt{-a_i^3}\right] \\ \quad \times\left[\ln\left|\sqrt{-a_{i+1}(1-e_{i+1})} - \sqrt{D_{i+1}}\right|\right. \\ \quad \left. -\ln\left|\sqrt{-a_i(1-e_i)} - \sqrt{D_i}\right|\right], & a_i < 0 \end{cases} \tag{15}$$

The entry trajectory is always subject to some operational and safety constraints, which restrict the magnitude of the drag acceleration. These constraints define a region, known as the entry corridor, in which the trajectory should lie. In terms of the constraints on the nodes D_i, they can be represented by

$$D_{\min}(e_i) \le D_i \le D_{\max}(e_i), \qquad i = 1, \ldots, n \tag{16}$$

For given e_i, values $D_{\min}(e_i)$ and $D_{\max}(e_i)$ are known. Several typical constraints will be discussed in the next section. But the constraints (16) on D_i can be easily converted by a transformation

$$D_i = 0.5[D_{\max}(e_i) + D_{\min}(e_i)] + 0.5[D_{\max}(e_i) - D_{\min}(e_i)]\sin x_i \tag{17}$$

where x_i is a new unconstrained parameter that defines D_i. Now the problem of determining the x_i (or, equivalently, D_i) becomes a parameter optimization problem subject to the constraint $s = s_{\text{ref}}$ for a given range s_{ref}. Because the analytical expressions for the cost function and constraint are available, the required optimal drag acceleration profile can be obtained very efficiently onboard when necessary. Also, when only minor adjustments are needed on the drag profile, the linearized ranging technique employed in the Shuttle guidance,[2] which adjusts only one segment of the drag profile at a time while keeping the rest unchanged, is still applicable. For instance, to null a range error δs by adjusting the ith node D_i, the required change in D_i is given by

$$\delta D_i = \delta s\left(\frac{\partial \Delta s_{i-1}}{\partial D_i} + \frac{\partial \Delta s_i}{\partial D_i}\right)^{-1} \tag{18}$$

where the partial derivatives are evaluated along the reference profile.

III. Regularization of the Optimization Problem

A closer examination of the preceding optimization problem in the sense of calculus of variations reveals a shortcoming of the problem formulation: The optimal drag profile thus obtained may consist a portion on the boundary of the entry corridor defined by Eq. (16), and a discontinuity in the optimal drag profile is usually present. To be more precise, we state the properties in a summary.

Proposition: Let $D^*(e)$ be the solution to the variational optimization problem formulated in the preceding section, which can be formally stated as

$$\min_{D(e)} J = \min_{D(e)} \int_{e_0}^{e_f} \sqrt{\frac{1-e}{D(e)}}\,\mathrm{d}e \tag{19}$$

$$\int_{e_0}^{e_f} \frac{1}{D(e)}\,\mathrm{d}e = s_f \tag{20}$$

$$D_{\min}(e) \le D(e) \le D_{\max}(e) \tag{21}$$

where $0 \leq e_0 < e_f < 1$ and s_f are prescribed and $D_{\max}(e)$ and $D_{\min}(e)$ are given smooth functions.

1) If there exists an e, $e_0 < e < e_f$, such that $D_{\max}(e) < (e_f - e_0)[1 - 0.5(e_f + e_0)]/s_f(1 - e)$, the constraints (21) will be active along D^* at some points in (e_0, e_f).

2) Suppose that $e_2 < e_f$ is a point where D^* leaves the boundary $D^* = D_{\max}$. If $D'_{\max}(e_2) < D_{\max}(e_2)/(1 - e_2)$, where the prime indicates differentiation with respect to e, then $D^*(e)$ has a discontinuity at e_2, jumping from $D_{\max}(e_2)$ at e_2^- to a point where $D_{\min}(e_2) \leq D^*(e_2^+) < D_{\max}(e_2)$.

The proof is given in the Appendix. For typical entry flight, $e_0 \approx 0.5, e_f \approx 1, s_f \approx 0.8$, and $D_{\max} < 1.5$. Thus, $(e_f - e_0)[1 - 0.5(e_f + e_0)]/s_f(1 - e) > D_{\max}$ will be true for $e > 0.9$. Numerical examples, as will be seen in the next section, suggest that the constraints (21) will usually become active on $D^* = D_{\max}$ and $D^* = D_{\min}$ in finite intervals. Note that the second property is valid no matter whether $D^* = D_{\max}$ only at some isolated points or in a finite interval. Both of these properties are not desirable. The first means that the vehicle will likely fly on part of the boundary of the entry corridor where no margin of error is allowed; the second simply indicates that the optimal drag profile may not be flyable by an actual vehicle. The discontinuity in D^* is an indication that the optimization problem was not properly posed. A standard method to correct such a defect is frequently referred to as Tikhonov regularization.[7] In this approach, an appropriate regularization term is added to the cost functional. The regularized problem then has additional smoothness properties, yet the solution of the regularized problem can be made arbitrarily close to that of the original problem. To this end, the cost functional is modified to be

$$\min_{D(e)} J = \min_{D(e)} \int_{e_0}^{e_f} \left\{ \sqrt{\frac{1-e}{D(e)}} + \varepsilon [D'(e)]^2 \right\} \mathrm{d}e \tag{22}$$

where the regularization parameter $\varepsilon > 0$ is a preselected small constant. Clearly, now the minimization of Eq. (22) prevents $D^*(e)$ from varying too fast, thus eliminating discontinuities. The value of ε can be adjusted to shape $D^*(e)$, depending on the particular entry corridor. With the piecewise-linear parametrization of $D(e)$, the problem again has analytical expressions for the cost function resulted from Eq. (22) and the isoperimetric constraint (20). The resulting parameter optimization problem to be solved numerically can now be stated as

$$\min_{D_i,\ 2 \leq i \leq n-1} J = \min_{D_i,\ 2 \leq i \leq n-1} \left\{ \sum_{i=1}^{n-1} \Delta J_i + \varepsilon \sum_{i=1}^{n-1} \left[\frac{(D_{i+1} - D_i)^2}{e_{i+1} - e_i} \right] \right\} \tag{23}$$

$$\sum_{i=1}^{n-1} \Delta s_i = s_f \tag{24}$$

$$D_{\min}(e_i) \leq D_i \leq D_{\max}(e_i) \tag{25}$$

$$D_1 = D_0, \qquad D_n = D_f \tag{26}$$

where Δs_i and ΔJ_i are still given by Eqs. (11) and (15), respectively, and D_0 and D_f are specified by conditions at the beginning and the end of the entry flight.

IV. Optimal Drag Profiles for an RLV

The RLV model used here, much like the configuration examined in Ref. 1, is a vertical-takeoff, horizontal-landing, winged-body single-stage concept studied at the NASA Marshall Space Flight Center.[8] The aerodynamic control surfaces are ailerons, elevons, body flap, and tip fins. Figure 1 gives a sketch of the configuration of the vehicle. For entry flight, the mass of the vehicle is set to be $m = 104{,}305$ kg (230,000 lb). The reference area $S = 391.22$ m^2. The aerodynamic coefficient C_L and C_D for the basic vehicle are given in tabulated data as functions of Mach number and angle of attack α. For the reference drag profile design in this section, the coefficients are approximated by fitting the data in hypersonic regimes with

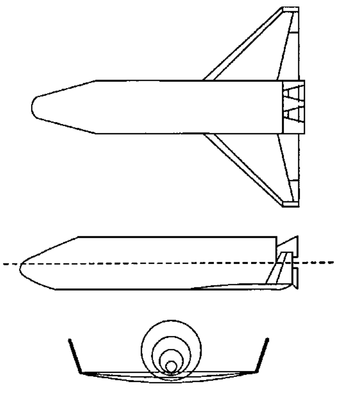

Fig. 1 RLV configuration.

$$C_L = -0.041065 + 0.016292\alpha + 0.00026024\alpha^2 \tag{27}$$

$$C_D = 0.080505 - 0.03026 C_L + 0.86495 C_L^2 \tag{28}$$

where α is in degrees. For this study, the angle of attack is scheduled with respect to velocity. It is first held at a constant of $\alpha = 40$ deg from the atmospheric entry ($v = 7450$ m/s) to $v = 4570$ m/s for thermal protection, and then reduced to 14 deg monotonically from $v = 4570$ m/s to $v = 760$ m/s where the handover to the terminal area guidance takes place. The entry corridor is usually defined by thermal, structural, and operational constraints. The ones considered here in dimensionless variables are as follows.

1) Heating rate constraint:

$$\sqrt{\frac{\rho}{\rho_0}} \left(\frac{\sqrt{R_0 g_0}}{v_{\text{ref}}} \right)^3 V^3 \leq \frac{\dot{q}_{\max}}{C_q} = 3.305 \times 10^9 \tag{29}$$

where $\rho_0 = 1$ kg/m^3, $v_{\text{ref}} = 1$ m/s, and the heat flux transmission coefficient $C_q = 1.65 \times 10^{-4}$ W/m^2. This corresponds to a maximum stagnation-point heating rate of $\dot{q}_{\max} = 544{,}300$ W/m^2 based on a reference sphere of radius of 1 m.

2) Load factor constraint in body-normal direction:

$$L \cos\alpha + D \sin\alpha \leq n_{\max} = 2\ (g) \tag{30}$$

where L is the lift acceleration in g.

3) Equilibrium glide constraint (at $\sigma = 0$): Set $\dot{\gamma} = 0$ at $\sigma = 0$ to get the minimum drag acceleration level

$$(C_D/C_L)[(1/r^2) - (V^2/r)] \leq D \tag{31}$$

4) Dynamic pressure constraint:

$$D \leq \frac{\bar{q}_{\max} S C_D}{m g_0} \tag{32}$$

where $\bar{q}_{\max} = 16{,}280$ (N/m^2) is the maximum allowable dynamic pressure.

With r approximated by an average value $\bar{r}$, all of the preceding constraint boundaries can be expressed in the e–D space, and they specify the entry corridor in which the drag profile must lie.

We parameterize $D(e)$ by 20 equally spaced piecewise-linear segments. The first two nodes $D_1 = 0.11$ and $D_2 = 0.66$ are prescribed to match the conditions resulted from atmospheric entry at an altitude of 120 km, $v_0 = 7450$ m/s (corresponding to $e_0 = 0.53687$), and $\gamma_0 = -0.5$ deg; the last node $D_{21} = 0.57$ is specified for a desired drag level at an altitude of 25 km and $v = 760$ m/s ($e_f = 0.99148$). The rest of the nodes are optimized using the analytical expressions derived in the preceding section.

First, we set $\varepsilon = 0$ in the cost function (23). This constrained parameter optimization problem (23–26) is solved by a sequential quadratic programming method.[9] The bounds on the nodes D_i by the entry corridor boundaries are accounted for by the transformation (17). Figure 2 shows the entry corridor and three optimal drag

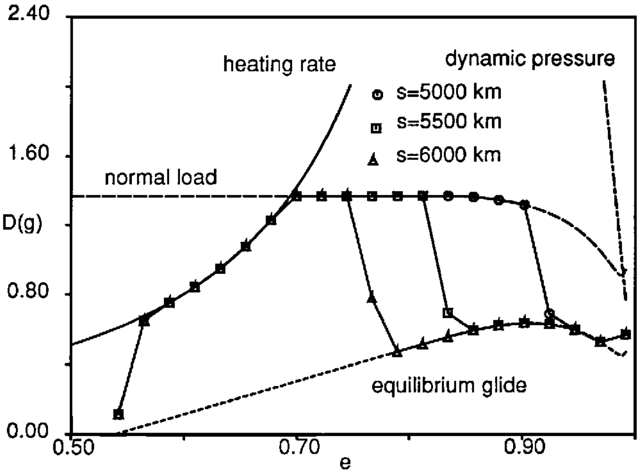

Fig. 2 Optimal drag profiles, $\varepsilon = 0$.

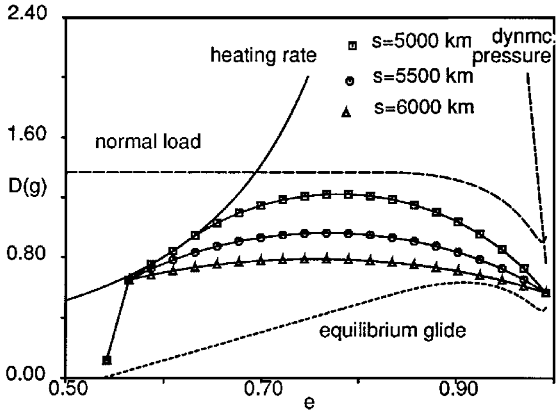

Fig. 3 Optimal drag profiles, $\varepsilon = 0.1$.

profiles corresponding to downrange distances of 5000, 5500, and 6000 km from the entry to e_f, respectively. As the Proposition indicates, which applies to the case where $\varepsilon = 0$, the common feature for these profiles is that the constraint $D = D_{\max}$ is active in the low-energy region for an extended period so as to minimize the accumulated heat [cf. Eq. (13)]. Even though the piecewise-linear continuous parametrization of $D(e)$ does not allow discontinuities, all of the solutions have a very rapid switching when the drag profiles leave the upper bound of the entry corridor, clearly indicating the existence of the jumps predicted by the Proposition [note that $D'_{\max} \approx 0$, thus is less than $D_{\max}(e)/(1-e)$ at the points where D^* leaves $D^* = D_{\max}$, a condition required by the Proposition].

Next, let $\varepsilon = 0.1$. The parameter optimization problem (23–26) is resolved. Figure 3 presents the three drag profiles obtained. The three new optimal profiles are much better behaved and well inside the entry corridor, thus can be tracked by the RLV easily. Compared to the case where $\varepsilon = 0$, the largest increase in the heat load according to Eqs. (14) and (15) is about 3.6% among the three trajectories, which seems to be a very acceptable penalty to pay on the performance index in exchange for the much more realistic trajectories. It should be mentioned that the problem is found to be quite insensitive to the choice of ε. For any $\varepsilon \in [0.1, 10]$, the solutions are virtually the same.

V. Trajectory Control Law

Once the reference drag acceleration profile is determined, the vehicle must be controlled to follow the reference profile closely. When the angle-of-attack profile is prescribed for the cross-range and terminal area guidance requirements, the trajectory control is primarily achieved by bank angle modulation. Linear feedback controls have been used.[2,5] More recently, a nonlinear control law based on the feedback linearization method is examined.[6]

We will also take a nonlinear, but different, approach for the trajectory control law design. This approach is based on a nonlinear predictive control concept developed in a series of recent papers.[10–12] Beginning with the complete nonlinear equations (1–3), we let the state vector $\boldsymbol{x} = \{r \;\; V \;\; \gamma\}^T$ and u be the control. The output variable is the actual drag acceleration $y = D(\boldsymbol{x})$. The output is to be controlled to track a given function of the state $y^* = D^*(\boldsymbol{x})$. [This is different from the formulation in Refs. 10–12, where an explicit function of time $y^*(t)$ is given as the desired output.] In the entry guidance problem, $D^*(\boldsymbol{x}) = D^*(e)$ is the reference drag profile. Assume constant C_D and an exponential atmosphere $\rho = \rho_0 e^{-(r-R_0)/h_s}$, where h_s is the scale height normalized by R_0. By the definition of D

$$\dot{D} = D[-(\dot{r}/h_s) + (2\dot{V}/V)] \tag{33}$$

$$\begin{aligned}\ddot{D} &= [(\dot{D}^2/D) - (2D\dot{V}^2/V^2) - (D/h_s)a_r(\boldsymbol{x}) + (2D/V)a_V(\boldsymbol{x})] \\ &\quad + D[(2/V)b_V(\boldsymbol{x}) - (1/h_s)b_r(\boldsymbol{x})]u \triangleq a_D(\boldsymbol{x}) + b_D(\boldsymbol{x})u\end{aligned} \tag{34}$$

where $a_r(\boldsymbol{x})$, $b_r(\boldsymbol{x})$, $a_V(\boldsymbol{x})$, and $b_V(\boldsymbol{x})$ are the terms defined in the expressions of $\ddot{r} = a_r(\boldsymbol{x}) + b_r(\boldsymbol{x})u$ and $\ddot{V} = a_V(\boldsymbol{x}) + b_V(\boldsymbol{x})u$,

$$\begin{aligned}a_r(\boldsymbol{x}) &= -[D + (\sin\gamma/r^2)]\sin\gamma + [(V^2/r) - (1/r^2)]\cos^2\gamma \\ b_r(\boldsymbol{x}) &= D\cos\gamma\end{aligned} \tag{35}$$

$$\begin{aligned}a_V(\boldsymbol{x}) &= -\dot{D} - [(V/r^3) - (1/Vr^4)]\cos^2\gamma + (2\dot{r}^2/Vr^3) \\ b_V(\boldsymbol{x}) &= -\frac{D\cos\gamma}{Vr^2}\end{aligned} \tag{36}$$

For piecewise-linear $D^*(e)$ as defined in Eq. (8), we have in the interval $[e_i, e_{i+1}]$

$$\dot{D}^* = a_i D V, \qquad \ddot{D}^* = a_i(\dot{D}V + D\dot{V}) \tag{37}$$

Following the formulation in Ref. 12, we define a new variable z dependent on the tracking error $\Delta D = D(\boldsymbol{x}) - D^*(\boldsymbol{x})$

$$z(\tau) = \Delta\dot{D} + 2\zeta\omega_n\Delta D + \omega_n^2\int_0^\tau \Delta D[\boldsymbol{x}(\mu)]\,\mathrm{d}\mu \tag{38}$$

where $\zeta > 0$ and $\omega_n > 0$ are two constants. By its definition, z is a first-order variable in the sense that $\dot{z}$ depends on u explicitly

$$\dot{z} = a_D(\boldsymbol{x}) + b_D(\boldsymbol{x})u + 2\zeta\omega_n\Delta\dot{D} + \omega_n^2\Delta D - \ddot{D}^* \tag{39}$$

Now following the predictive control method in Refs. 10 and 11, at an arbitrary τ, the change of z at the next instant $\tau + T$ for a time increment $T > 0$ is influenced by the current control $u(\tau)$, and the change may be predicted by a first-order Taylor series expansion

$$\begin{aligned}z(\tau + T) &\approx z(\tau) + T\dot{z}(\tau) \\ &= z(\tau) + T\big\{a_D[\boldsymbol{x}(\tau)] + b_D[\boldsymbol{x}(\tau)]u(\tau) + 2\zeta\omega_n\Delta\dot{D}[\boldsymbol{x}(\tau)] \\ &\quad + \omega_n^2\Delta D[\boldsymbol{x}(\tau)] - \ddot{D}^*[\boldsymbol{x}(\tau)]\big\}\end{aligned} \tag{40}$$

Because it is desired to drive z to zero (corresponding to $\Delta D = 0$), the current control $u(\tau)$ is found by minimizing the performance index

$$J = \tfrac{1}{2}z^2(\tau + T) \tag{41}$$

Replacing $z(\tau + T)$ by Eq. (40) and setting $\partial J/\partial u(\tau) = 0$ give a continuous, nonlinear feedback control law

$$u = -\frac{1}{Tb_D(x)}\big\{z + T\big[a_D(x) - \ddot{D}^* + 2\zeta\omega_n\Delta\dot{D} + \omega_n^2\Delta D\big]\big\} \tag{42}$$

The globally asymptotically stable tracking of D^* under the control law (42) for any $T > 0$, in the absence of control saturation, can be readily established by substituting Eq. (42) into Eq. (39) to arrive at

$$\dot{z} = -(1/T)z \tag{43}$$

Thus $z \to 0$ exponentially with a time-constant T, and $\dot{z} \to 0$. From the definition of z, $\dot{z} = 0$ leads to

$$\Delta\ddot{D} + 2\zeta\omega_n\Delta\dot{D} + \omega_n^2\Delta D = 0 \tag{44}$$

Therefore, $\Delta D \to 0$ with a damping ratio of ζ and natural frequency of ω_n.

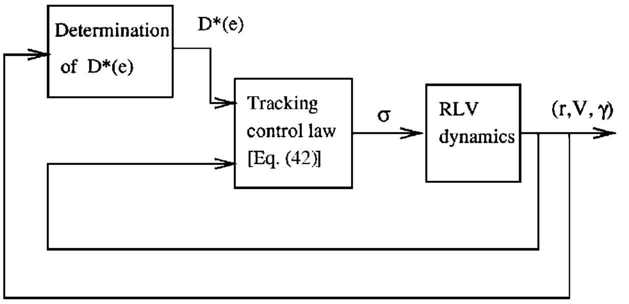

Fig. 4 Schematic diagram of the closed-loop guidance system.

A schematic diagram for the closed-loop guidance system is shown in Fig. 4. Based on the current energy level, the value of the reference drag acceleration $D^*(e)$ is determined (note that this block could also represent onboard generation of the reference drag profile D^* when needed). Then the trajectory control law (42) gives the desired bank-angle command $\cos\sigma = uC_D/C_L$, which in turn is used to steer the RLV.

Upon replacing z by its definition (38) in the control law (42), it is clear that this is a nonlinear proportional-integral-derivative (PID) control law. In the steady state when $z \to 0$, the control law reduces to the standard feedback linearization control

$$u = -\frac{1}{b_D(\boldsymbol{x})}\left[a_D(\boldsymbol{x}) - \ddot{D}^* + 2\zeta\omega_n\Delta\dot{D} + \omega_n^2\Delta D\right] \qquad (45)$$

which is a proportional-plus-derivative control law. Both control laws can achieve globally asymptotically stable tracking of D^* in ideal situation. The difference between control laws (42) and (45), however, has a significant practical impact. In the implementation of the entry guidance, the information on $\dot{D}$ is obtained through the altitude rate [Eq. (33)] to avoid the noise associated with differentiation of D (Ref. 2). Because the error in determining $\dot{r}$ using an inertial navigation system is unstable, a steady-state error in drag acceleration is induced as a result. The integral term in the control law (42) will eliminate this steady-state error. The Shuttle trajectory control law is essentially a linearized version of Eq. (45), but an integral term is added in it to address the problem of steady-state drag error.[2] An integral feedback term can also be added to the feedback linearization control law (45) to reduce the steady-state drag errors effectively. In further evaluation of the control law performance, the integral term should be included because of its practical importance, as will be demonstrated by numerical tests in the next section.

Note that in the argument used to show the asymptotic tracking stability, the reference drag profile D^* is implicitly assumed to be C^2 globally. The piecewise-linear parametrization in the preceding section does not satisfy this assumption. But for all practical purposes, the discontinuities in $\dot{D}^*$ and $\ddot{D}^*$ only cause slight tracking performance degradation in the immediate vicinity of the corners. Similarly, the dependence of the control law (42) on flight-path angle γ can be eliminated by letting $\cos\gamma = 1$ and $\sin\gamma = 0$, and this will not have any noticeable adverse effects on the control law performance.

Another issue is that by its definition the control u is bounded by the minimum and maximum allowable bank angles, and the lift-to-drag ratio at each instant, so that

$$U_{\min}[\boldsymbol{x}(\tau)] \le u(\tau) \le U_{\max}[\boldsymbol{x}(\tau)] \qquad (46)$$

where the bounds are obviously state dependent. A saturater defined at each instant τ as

$$\mathrm{sat}(w) = \begin{cases} U_{\max}[\boldsymbol{x}(\tau)], & w \ge U_{\max}[\boldsymbol{x}(\tau)] \\ w, & U_{\min}[\boldsymbol{x}(\tau)] < w < U_{\max}[\boldsymbol{x}(\tau)] \\ U_{\min}[\boldsymbol{x}(\tau)], & w \le U_{\min}[\boldsymbol{x}(\tau)] \end{cases} \qquad (47)$$

can be applied to the right-hand side of the control law (42) to ensure the control constraints. When the control law (42) saturates according to Eq. (47), it is still optimal in the sense of minimizing Eq. (41) within the bounds (46), because the cost (41) with $z(t+T)$ approximated by Eq. (40) is a convex quadratic function of the scalar $u(\tau)$. In contrast, a feedback linearization control law in the presence of saturation will not render meaningful control.

The parameter T in the control law (42) has a clear physical meaning: $1/T$ is the controller gain, and T is the time constant of the transient process [Eq. (43)]. Note that T is not required to be a constant necessarily. Thus, a larger T may be used when initial errors are large to avoid control saturation, and a smaller T may be used for quick tracking convergence when errors are small. An automated optimal tuning method is proposed in Ref. 13. But in the simulation presented in the next section, a properly selected constant T is found to work satisfactorily.

VI. Numerical Evaluation of Tracking Performance

To evaluate the performance of the control law (42) in tracking the piecewise-linear reference profiles obtained in Sec. IV, control law (42) is applied to the full point-mass equations of motion (1–3) with the parameter $T = 0.005$ in τ (4 s in real time). The damping ratio is set at $\zeta = 0.7$, and $\omega_n = \sqrt{(R_0/g_0)}/15$ (dimensionless, corresponding to a natural frequency of $\frac{1}{15}$ s^{-1} in real time). Although the lift and drag coefficients C_L and C_D are approximated by Eqs. (27) and (28) in the solution for the reference profile, and C_D is treated as a constant in the control law derivation, in this simulation C_L and C_D are found by table lookup as functions of angle of attack and Mach number, where the speed of sound is obtained by interpolating the data from the 1976 U.S. Standard Atmosphere. The density of the 1976 Standard Atmosphere in the altitude ranges under consideration is closely matched by the exponential atmosphere $\bar{\rho} = 1.752\, e^{-R_0(r-1)/6700}$ (kg/m^3), but the density used in the simulation is actually

$$\rho = \bar{\rho}\left\{1 - 0.4\left(\frac{h-20}{100}\right)\cos\left[2\pi\left(\frac{120-h}{50}\right)\right]\right\} \qquad (48)$$

to emulate density fluctuations from the standard atmosphere, where h is the altitude in kilometer.

Figure 5 shows how the actual (simulated) drag profiles follow the three reference profiles plotted in Fig. 3, which will be called, according to their ranges, the short, medium, and long trajectories in the following. It is evident that the actual drag profiles track the references very well, except in the vicinity of the first corner point on the reference profiles, where the discontinuities in the slopes of the reference profiles cause some small deviations. As an evaluation of the range accuracy of the guidance scheme, the actual ranges are obtained by integrating Eq. (6) along the guided trajectories, and compared with the specified ranges (5000, 5500, and 6000 km, respectively). The range errors are 0.5, 0.74, and 0.52 km. It should be mentioned that the effects of bank reversals for cross-range control and the rotation of the Earth were not considered in the described simulations.

Figure 6 depicts the typical bank angle history (along the medium-range trajectory). From the initial penetration of the atmosphere at 120 km to the activation of the entry guidance, the bank angles are set at zero. The guidance scheme in this simulation is activated when the drag acceleration reaches a threshold value of 0.6 g. The spikes

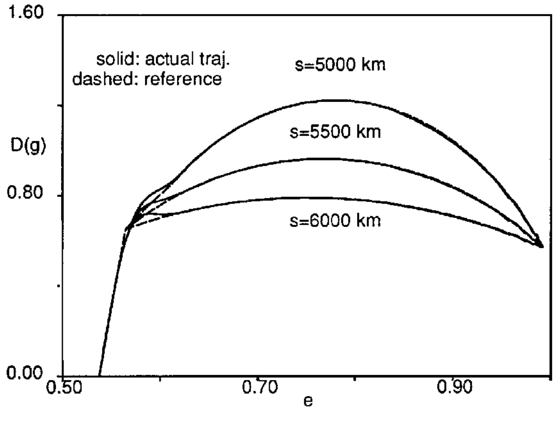

Fig. 5 Drag profiles under control law (42).

in the bank angle history are caused by the slope discontinuities of the reference drag profile. If the commanded bank angle is also desired to observe the maximum roll-rate limit of the RLV, minor modifications in the control law and the saturater (47) can be made, and the modified guidance law will guarantee that both the rate and the magnitude of the bank angle commands are within the specified limits. For detailed discussion on simultaneously enforcing control and control-rate limits, the reader is referred to Ref. 14.

Figure 7 presents the variation of altitude history along the medium trajectory. The typical cutoff altitude is just under 28 km, and the velocity at that altitude is about 720 m/s. Figures 8–10 illustrate the variations of α vs velocity; C_L, C_D, and C_L/C_D vs α and vs energy along the same trajectory.

It is pointed out in Sec. V that the error in determining the altitude rate using an inertial navigation system will cause a steady-state drag error. The integral term in the control law (42) is expected to

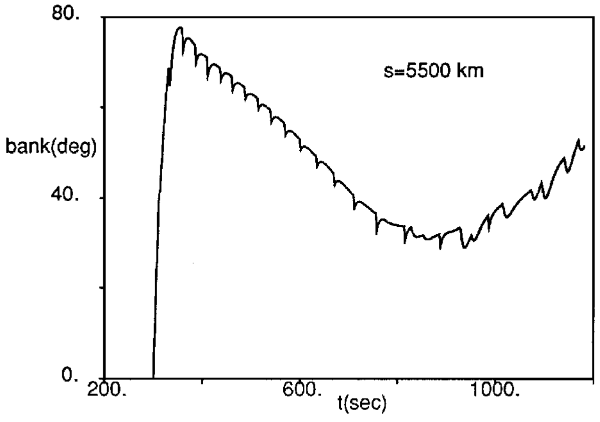

Fig. 6 Bank angle history along the medium trajectory.

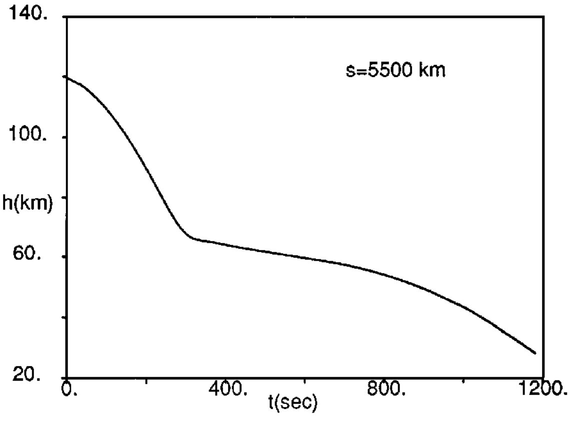

Fig. 7 Altitude history along the medium trajectory.

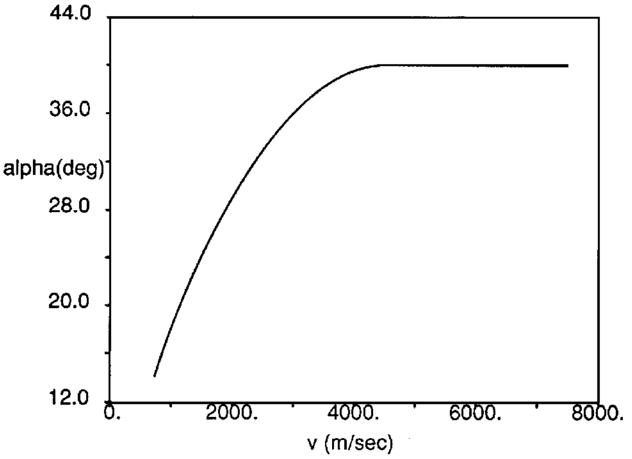

Fig. 8 Angle-of-attack variation along the medium trajectory.

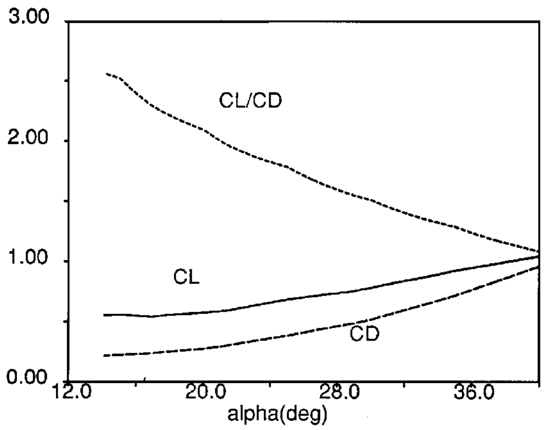

Fig. 9 C_L, C_D, and C_L/C_D variations with respect to α.

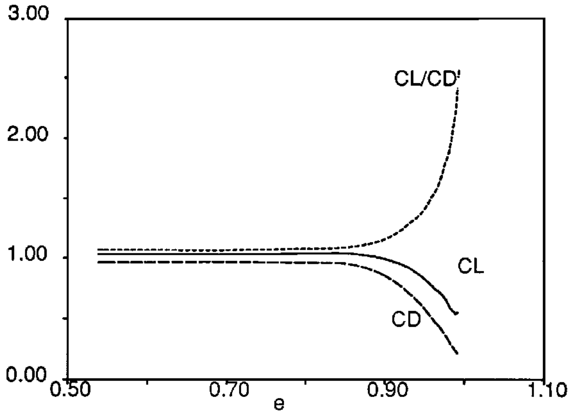

Fig. 10 C_L, C_D, and C_L/C_D variations with respect to energy.

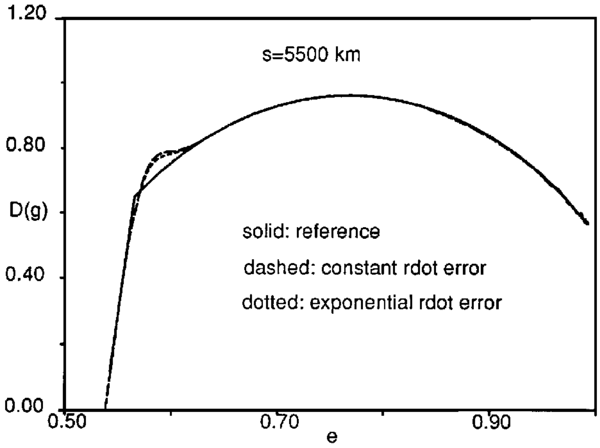

Fig. 11 Drag profiles under control law (42) with altitude rate $\dot{r}$ errors.

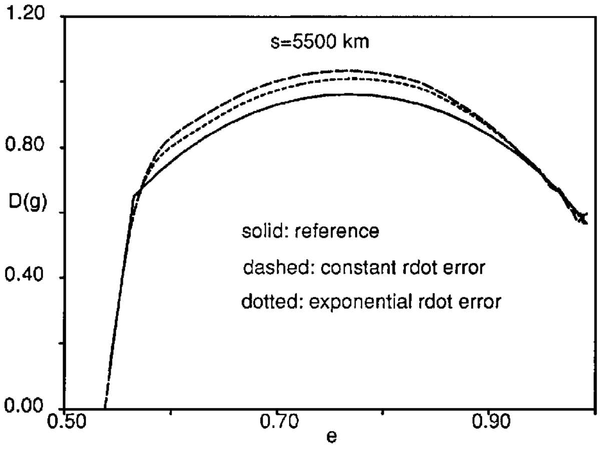

Fig. 12 Drag profiles under control law (45) with altitude rate $\dot{r}$ errors.

eliminate this error. For a test, a constant error $\delta\dot{r}$ of 20 m/s and then a growing error of $\delta\dot{r} = 5e^{[\sqrt{(2g_0/R_0)}]t}$ (m/s) are introduced in the simulation. The latter represents the unstable mode in the vertical channel of an inertial navigation system. The control law is given $\dot{r}+\delta\dot{r}$ in place of $\dot{r}$, especially for the calculation of $\dot{D}$ from Eq. (33). But accurate feedback of D is assumed. Figure 11 shows the actual drag profiles under control laws (42), tracking the long reference trajectory. The actual drag profiles have overshoots because of the altitude rate errors and the discontinuity in the slope of the reference profile, but quickly recover and converge to the reference profile. The range errors for the two cases are -6.17 and -5.3 km. For the same altitude rate errors, the drag profiles under the control law (45) are plotted in Fig. 12 for comparison. Steady-state drag errors are clearly seen. The range errors are -151.5 and -105.5 km, respectively.

VII. Conclusions

The entry guidance for the future reusable launch vehicle is likely to build on the successful Shuttle entry guidance concept. This paper studies several improvements that could further enhance the performance and accuracy of the entry guidance system. The first is to design the optimal reference drag acceleration profile in piecewise-linear functions of the energy, instead of the velocity as in the Shuttle guidance. With this simple modification, analytical range prediction based on the drag profile is preserved and more accurate, and the accumulated heat load along the trajectory can also be analytically integrated. A Tikhonov regularization method is used to further shape the reference drag profiles for better feasibility. These properties make off-line design of the reference drag profiles to satisfy the given range requirement and minimize the heat load very efficient and on-line design of these reference profiles possible. To track the reference drag profile, a nonlinear feedback trajectory control law is proposed. This control law is essentially a nonlinear PID control law, which guarantees, in the absence of control saturation, globally asymptotically stable tracking of the reference drag profile in the entry corridor. In the presence of navigation errors such as altitude rate errors, which will cause steady-state drag error, the control law is shown to be able to eliminate the drag error and still ensure good tracking of the reference drag profile. Numerical results are provided for a conceptual RLV to demonstrate the optimal design of reference drag profiles and effectiveness of the trajectory control law.

Finally, it should be noted that although the numerical experiments were done for a horizontal-landing, winged-body RLV configuration, the basic methodology is equally applicable to the lifting-body configuration of the designated X-33/RLV vehicle.

Appendix: Proof of the Proposition

The proof is best done by contradictions. For the proof of the first part of the Proposition, suppose that the constraints (21) are not active anywhere in (e_0, e_f) along D^*. In this case the augmented integrand function for the constrained variational problem (19–21) is the same as for the unconstrained one, which is just

$$L = \sqrt{[(1-e)/D(e)]} + \mu[(1/D) - z'] \tag{A1}$$

where μ is a multiplier and $z' = \mathrm{d}z/\mathrm{d}e$ for an auxiliary variable z. Because L is independent of D', the necessary conditions for the variational solution (known as the Euler equations in the calculus of variations) consist of one differential equation

$$\frac{\partial L}{\partial z} - \mathrm{d}\left(\frac{\partial L}{\partial z'}\right)\Bigg/\mathrm{d}e = 0 \tag{A2}$$

and an algebraic equation

$$\frac{\partial L}{\partial D} = 0 \tag{A3}$$

From Eq. (A2) $\mathrm{d}\mu/\mathrm{d}e = 0$, thus $\mu = \text{const}$. By Eq. (A3) we have

$$D^* = 4\mu^2/(1-e) \tag{A4}$$

The constant $4\mu^2$ can be determined by the satisfaction of the isoperimeric constraint (20), which leads to

$$D^* = \frac{(e_f - e_0)[1 - 0.5(e_f + e_0)]}{s_f(1-e)} \tag{A5}$$

However, the condition given in the Proposition, $D_{\max}(e) < (e_f - e_0)[1 - 0.5(e_f + e_0)]/s_f(1-e)$ for some $e_0 < e < e_f$, would mean that $D_{\max}(e) < D^*(e)$ for such an e. Thus, the constraints (21) are violated. Therefore, the constraints (21) must be active along D^* at some points in (e_0, e_f).

For the proof of the second part of the Proposition, suppose that $D^*(e)$ is continuous at $e_2 < e_f$ [so that $D^*(e_2^-) = D^*(e_2^+) = D_{\max}(e_2)$]. Because e_2 is the point where $D^*(e)$ leaves $D = D_{\max}$, there exists a $\Delta e > 0$ such that

$$D_{\min}(e) < D^*(e) < D_{\max}(e) \tag{A6}$$

for all $e \in (e_2, e_2 + \Delta e) \subset [e_2, e_f]$. Thus, D^* takes the form of the differentiable solution (A4) in this interval, and $D^{*\prime}(e_2^+) = 4\mu^2/(1-e_2)^2 = D^*(e_2^+)/(1-e_2) = D_{\max}(e_2)/(1-e_2)$. Because by the condition of the Proposition $D'_{\max}(e_2) < D_{\max}(e_2)/(1-e_2) = D^{*\prime}(e_2^+)$, there must exist a $\delta > 0$ such that $D^*(e) > D_{\max}(e)$ for any $e \in (e_2, e_2+\delta)$, which violates constraint (21) [or (A6)]. Hence, $D^*(e)$ cannot be continuous at e_2. Thus, $D^*(e_2^+)$ must be such that

$$D_{\min}(e_2) \le D^*(e_2^+) < D_{\max}(e_2)$$

The proof is completed.

Acknowledgments

The author thanks John Hanson and Wade Shrader at the NASA Marshall Space Flight Center for providing the vehicle data used in this study. Technical discussions with John Hanson are gratefully acknowledged.

References

[1] Stanley, D. O., Engelund, W. C., Lepsch, R. A., McMillin, M., Wurster, K. E., Powell, R. W., Guinta, T., and Unal, R., "Rocket-Powered Single-Stage Vehicle Configuration Selection and Design," *Journal of Spacecraft and Rockets*, Vol. 31, No. 5, 1994, pp. 792–798.

[2] Harpold, J. C., and Graves, C. A., "Shuttle Entry Guidance," *Journal of the Astronautical Sciences*, Vol. 37, No. 3, 1979, pp. 239–268.

[3] Harpold, J. C., and Gavert, D. E., "Space Shuttle Entry Guidance Performance Results," *Journal of Guidance, Control, and Dynamics*, Vol. 6, No. 6, 1983, pp. 442–447.

[4] Jänsch, C., and Markl, A., "Trajectory Optimization and Guidance for a Hermes-Type Reentry Vehicle," *Proceedings of the AIAA Guidance, Navigation, and Control Conference* (New Orleans, LA), AIAA, Washington, DC, 1991, pp. 543–553.

[5] Roenneke, A. J., and Markl, A., "Re-entry Control of a Drag vs. Energy Profile," *Journal of Guidance, Control, and Dynamics*, Vol. 17, No. 5, 1994, pp. 916–920.

[6] Mease, K. D., and Kremer, J.-P., "Shuttle Guidance Revisited Using Nonlinear Geometric Methods," *Journal of Guidance, Control, and Dynamics*, Vol. 17, No. 6, 1994, pp. 1350–1356.

[7] Morozov, V. A., *Regularization Methods for Ill-Posed Problems*, CRC Press, Boca Raton, FL, 1993, pp. 192–209.

[8] Anon., "Trajectory Design Data Package: Reference Mission 1 for WB-001," NASA Marshall Space Flight Center, Sept. 1994.

[9] Pouliot, M. R., "CONOPT2: A Rapidly Convergent Constrained Trajectory Optimization Program for TRAJEX," General Dynamics, Rept. GDC-SP-82-008, Convair Div., San Diego, CA, 1982.

[10] Lu, P., "Nonlinear Predictive Controllers for Continuous Systems," *Journal of Guidance, Control, and Dynamics*, Vol. 17, No. 3, 1994, pp. 553–560.

[11] Lu, P., "Optimal Predictive Control of Continuous Nonlinear Systems," *International Journal of Control*, Vol. 62, No. 3, 1995, pp. 633–649.

[12] Singh, S. N., Steinberg, M., and DiGirolamo, R. D., "Nonlinear Predictive Control of Feedback Linearizable Systems and Flight Control System Design," *Journal of Guidance, Control, and Dynamics*, Vol. 18, No. 5, 1995, pp. 1023–1028.

[13] Lu, P., "Nonlinear Systems with Control and State Constraints," *Optimal Control Applications and Methods* (to be published).

[14] Lu, P., "Tracking Control of Input–Output Feedback Linearizable Systems with Bounded Controls and Control Rates," *Proceedings of the 13th World Congress, International Federation of Automatic Control* (San Francisco, CA), Elsevier Science, Oxford, England, UK, 1996.